

This work was written as part of one of the author's official duties as an Employee of the United States Government and is therefore a work of the United States Government. In accordance with 17 U.S.C. 105, no copyright protection is available for such works under U.S. Law. Access to this work was provided by the University of Maryland, Baltimore County (UMBC) ScholarWorks@UMBC digital repository on the Maryland Shared Open Access (MD-SOAR) platform.

Please provide feedback

Please support the ScholarWorks@UMBC repository by emailing scholarworks-group@umbc.edu and telling us what having access to this work means to you and why it's important to you. Thank you.

**Measurement of the Iron Spectrum in Cosmic Rays
from 10 GeV/n to 2.0 TeV/n with the Calorimetric Electron Telescope
on the International Space Station SUPPLEMENTAL MATERIAL**

(CALET collaboration)

Supplemental material relative to “Measurement of the Iron Spectrum in Cosmic Rays from 10 GeV/n to 2.0 TeV/n with the Calorimetric Electron Telescope on the International Space Station with the Calorimetric Electron Telescope”

CHARGE MEASUREMENT

In Fig. S1 inclusive distributions of measured charges from flight data (FD) are compared, in two different energy bins, with Monte Carlo (MC) simulations from EPICS.

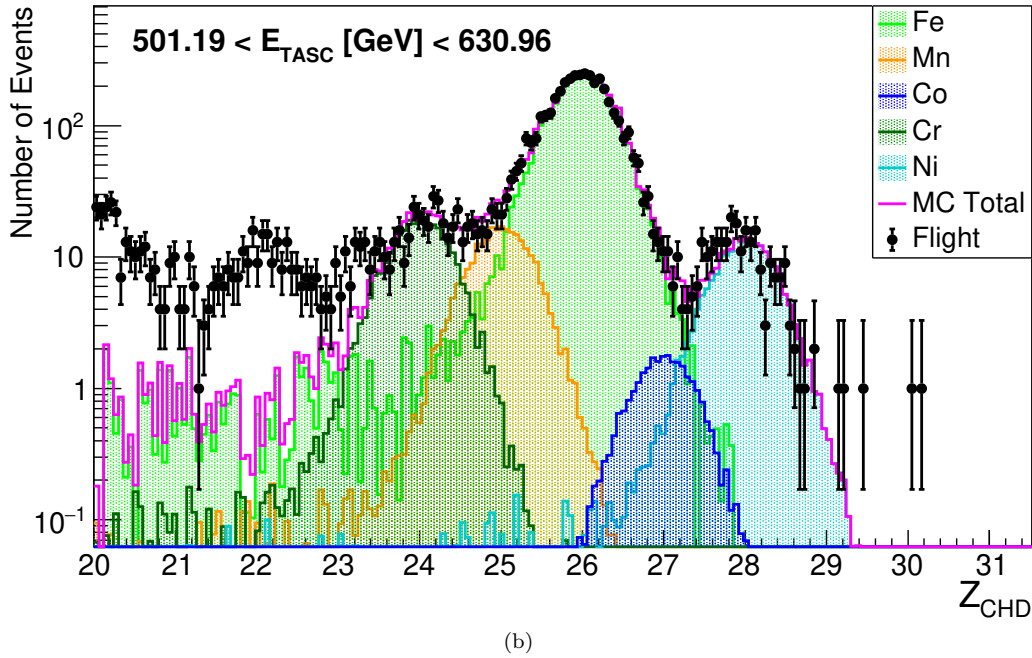
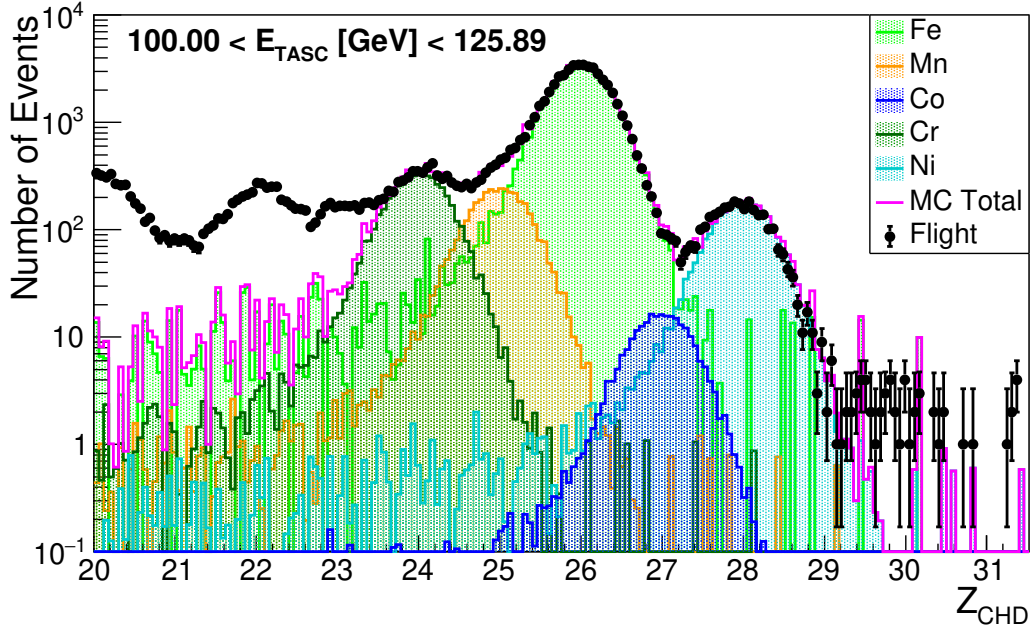


FIG. S1. Charge distributions from the combined charge measurement of the two CHD layers in the elemental region between Ca and Ge. Events are selected with $100 < E_{TASC} < 125$ GeV in (a) and $501 < E_{TASC} < 630$ GeV in (b). Flight data, represented by black dots, are compared with Monte Carlo samples including chromium, manganese, iron, cobalt and nickel. Titanium and vanadium are not included in MC because their contamination to iron data is negligible.

In Fig. S2, obtained with flight data, a cross-plot of the independent charge measurements provided by the two CHD layers shows a clear separation of iron candidates from the less abundant neighbor elements.

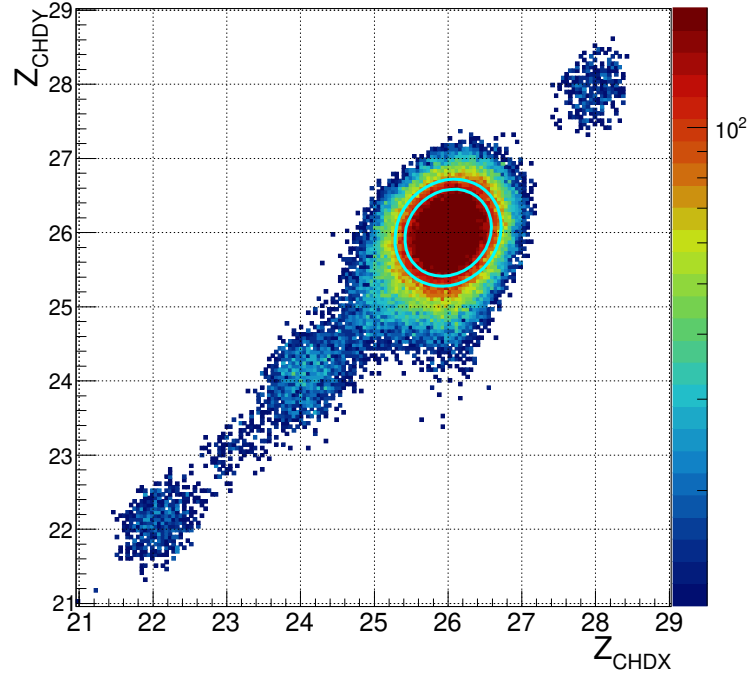


FIG. S2. Crossplot of Z_{CHDY} vs. Z_{CHDX} reconstructed charges in the elemental range between Ti ($Z = 22$) and Ni ($Z = 28$). Iron candidates are selected inside an ellipse with minor and major semi-axes $1.25 \sigma_x$ and $1.25 \sigma_y$, respectively, rotated clockwise by 45° . The maximum and the minimum elliptical selection are indicated by the cyan ellipses in the figure.

LIGHT QUENCHING IN THE TASC CRYSTALS

For nuclei with $Z > 10$, the TASC crystals undergo a light quenching phenomenon as is clearly visible in Fig. S3. In the same figure the position of the peak for a minimum-ionizing particle (MIP), generated by a non-interacting primary particle crossing the first TASC layer, is plotted as a function of Z^2 for nine elements ranging from O to Ni and selected from flight data. A “halo” model is used in the fit to parameterize the non-linearity of the scintillator’s response due to light quenching. The applied corrections on the signals from the plastic scintillators are based on the same model, as explained in [S1].

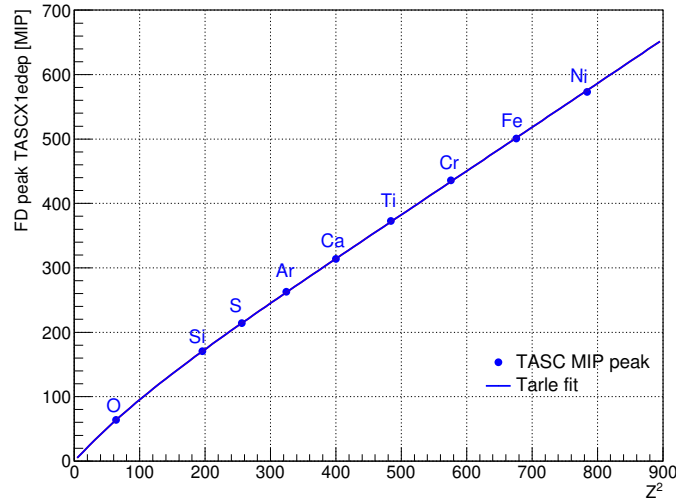


FIG. S3. Cross-plot of the minimum ionizing energy deposit in the first TASC layer as a function of Z^2 for nine elements ranging from O to Ni selected from flight data. Each element used in the fit is identified by its chemical label.

ADDITIONAL INFORMATION ON THE ANALYSIS

Efficiencies. The total efficiency and relative efficiencies (i.e., the efficiency of a given cut normalized to the previous cut) were studied extensively over the whole energy range covered by the iron flux measurement. The total selection efficiency from EPICS (blue open circles) and FLUKA (red filled circles) are shown in Fig. S4 as a function of total particle kinetic energy per nucleon.

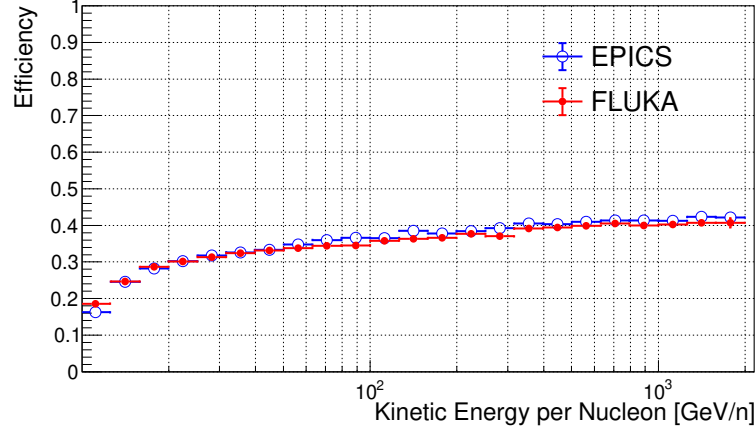


FIG. S4. Total selection efficiency for iron events as estimated with EPICS (blue open circles) and FLUKA (red filled circles) simulations.

The above efficiencies were validated by comparing distributions relevant to the selection of events, and obtained from flight data, with the same distributions generated by EPICS or FLUKA.

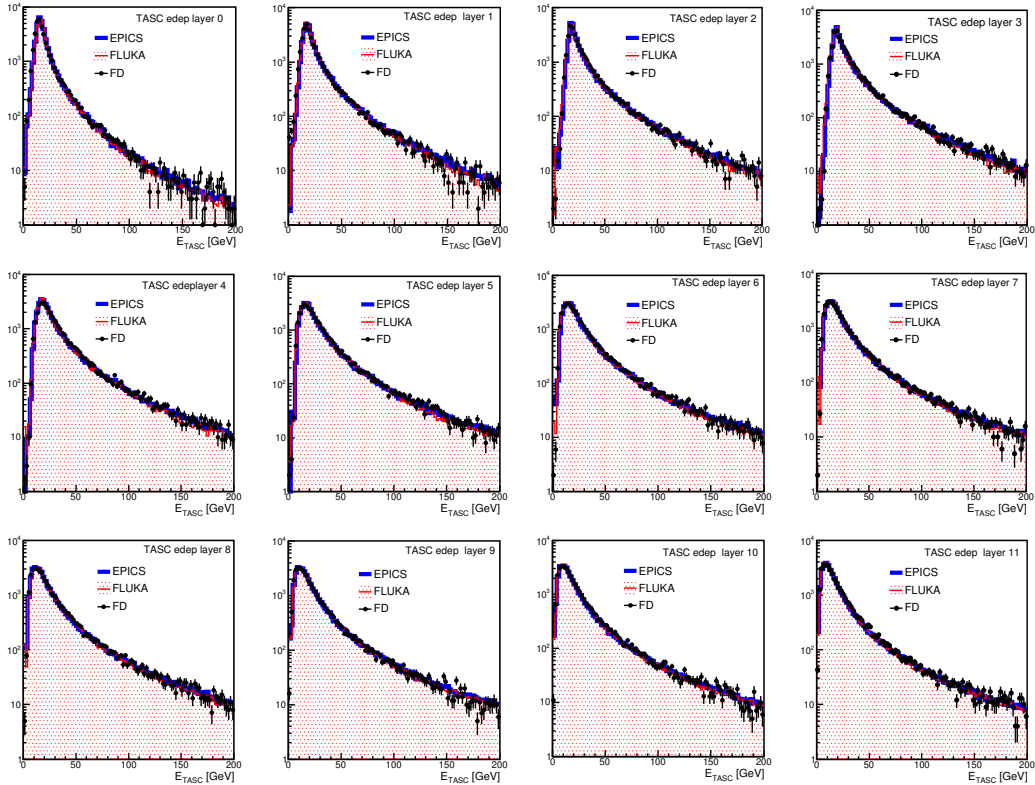


FIG. S5. Energy observed in each of the 12 layers of the TASC (black points) for the final sample of iron candidates from flight data. It is compared with pure samples of iron simulated by EPICS (blue) or FLUKA (red).

An example is given in Fig. S5 where the total energy observed in each layer of the TASC (black points) were plotted using the final sample of iron candidates, marginally contaminated by a residual background (estimated around 1%) due to elements with atomic number close to iron. Compared with pure iron samples simulated by EPICS (blue) or FLUKA (red), the distributions from the two MC were found to be consistent with each other and in fair agreement with flight data.

Interactions in the instrument. The amount of instrument material above the CHD is very small and well known. The largest significant contribution is limited to a 2 mm thick Al cover placed on top of the CHD. This amounts to $\sim 2.2\%$ radiation length and $5 \times 10^{-3} \lambda_I$. The material description in the MC is very accurate and derived directly from the CAD model. As CALET is sitting on the JEM external platform of the ISS, no extra material external to CALET is normally present within the acceptance adopted for the flux measurement. However, occasional obstructions caused by the ISS robotic arm operations may temporarily affect the FOV. Those rare periods are well identified and events discarded accordingly (a continuous monitoring is routinely done for gamma-ray analyses).

MC simulations were used to evaluate the iron survival probability after traversing both layers of the CHD and the material above. In order to check its consistency with flight data, the ratio $R = (\text{CHDX} \& \text{CHDY}) / \text{CHDX}$ (i.e. the fraction of iron candidates tagged by both CHD layers among those detected by the top charge detector) was plotted, as a function of the TASC energy, for selected iron candidates with measured charge in the range 25.5 - 26.5. In the upper panel of Fig. S6, R is shown in 15 bins of the TASC energy for both MC (R_{MC}) and FD (R_{FD}) with an average value around 90% and a flat energy dependence. The R_{MC}/R_{FD} double ratio (lower plot) shows a good level of consistency between the MC and flight data, within the errors. The total loss ($\sim 10\%$) of iron events interacting in the upper part of the instrument was taken into account in the total efficiency and its uncertainty included in the systematic error.

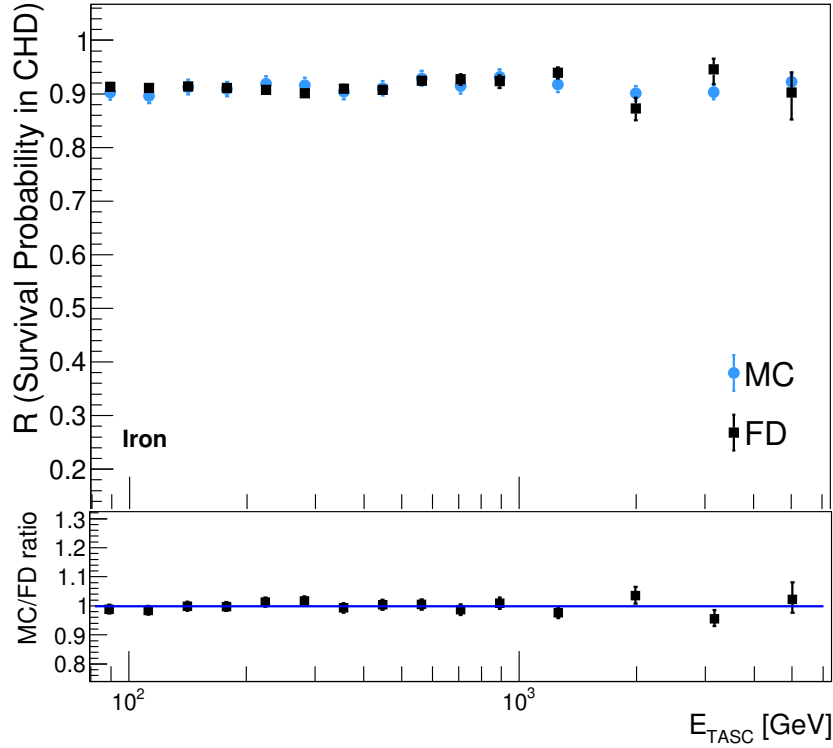


FIG. S6. Top panel: iron survival probability R as a function of energy for events crossing both layers of the CHD with flight data (black filled squares) and EPICS (blue filled circles); Bottom panel: ratio of R_{MC}/R_{FD} with the MC and flight data, respectively, fitted with a constant and consistent with unity within the error.

Background contamination. Background contamination of iron from neighbor elements is relatively small as shown in Fig. S7 as a function of the TASC energy. It is subtracted from the flux as explained in the main body of the paper.

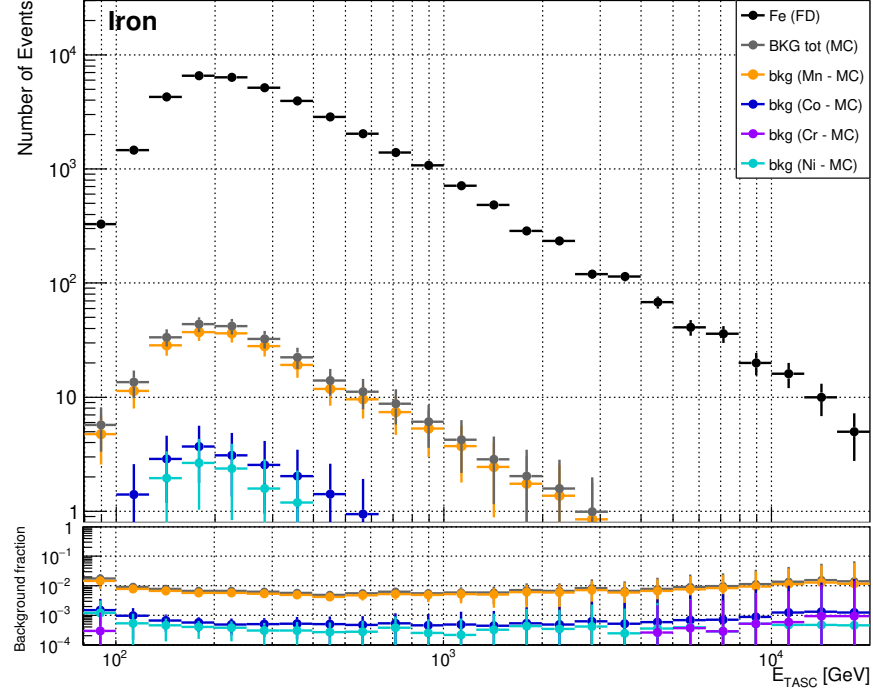


FIG. S7. Top panel: Differential distributions of the number of events in a given bin of calorimetric energy (E_{TASC} in GeV) for selected iron events in flight data (black dots) before the unfolding procedure and with background events from nuclei close to iron in atomic number. Bottom panel: Contamination from each nuclear species between $Z = 24$ and $Z = 28$ from the MC. The Monte Carlo events are weighted with a factor to reproduce a single power law spectrum with spectral index -2.6, and event selection is the same as for flight data. The resulting elemental charge distribution in each observed energy bin has been normalized to match the CHD charge distribution of flight data. The number of contaminant events is calculated by integration of all the MC events accepted by the iron charge selection.

Calorimetric energy, bin size, and unfolding. The energy response of the TASC was studied with MC simulations and compared with the results of measurements of the total particle energy vs beam momentum carried out at CERN. During one of the beam test campaigns of CALET at the SPS with an extracted primary beam of ^{40}Ar (150 GeV/c/n), beam fragments were generated from an internal target and guided toward the instrument along a magnetic beam spectrometer that provided an accurate selection of their rigidity and A/Z ratio. The relation between the observed TASC energy and the primary energy was measured for several nuclei up to the highest available energy (6 TeV total particle energy in the case of ^{40}Ar). After an offline rejection of a very small amount of beam contaminants from the data, the shape of the TASC total energy was found to be consistent with a Gaussian distribution [S2].

The correlation matrix used for the unfolding was derived from the simulations, using two different MC codes EPICS and FLUKA, and applying the same selection cuts as in the FD analysis. Three different binning schemes (4, 5, 10 equal log-bins /decade) have been applied. Two normalized unfolding matrices (with 4 and 10 bins/decade) derived from EPICS are shown in Fig. S8.

The aforementioned three binning schemes were applied to the iron flux analysis with the result shown in Fig. S9 where only statistical errors are shown. Within the errors, no statistically significant difference was found among the three fluxes.

Energy dependent systematic errors. A breakdown of energy dependent systematic errors stemming from several sources (as explained in the main body of the paper) and including selection cuts, charge identification, MC model, energy scale correction, energy unfolding, beam test configuration and shower event shape is shown in Fig. S10 as a function of kinetic energy per nucleon.

Iron flux normalization and spectral shape. The CALET iron flux and a compilation of available data, including

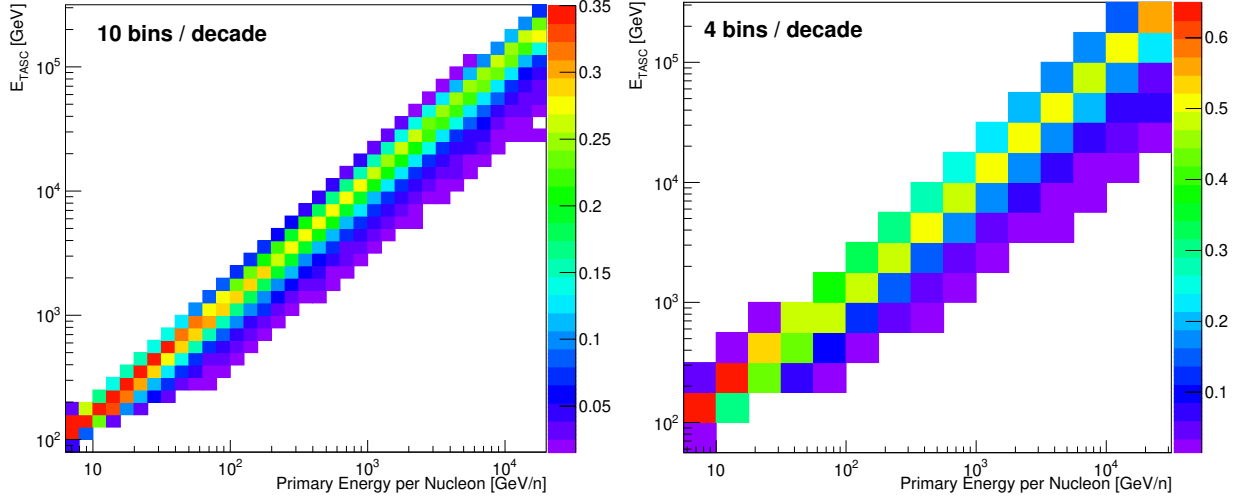


FIG. S8. Response matrix for iron derived from the MC simulations of the CALET flight model by applying the same selection as for flight data. The array is normalized so that the color scale is associated to the probability that iron candidates in a given bin of particle kinetic energy cover different intervals of E_{TASC} . Left: 10 bins/decade; Right: 4 bins/decade.

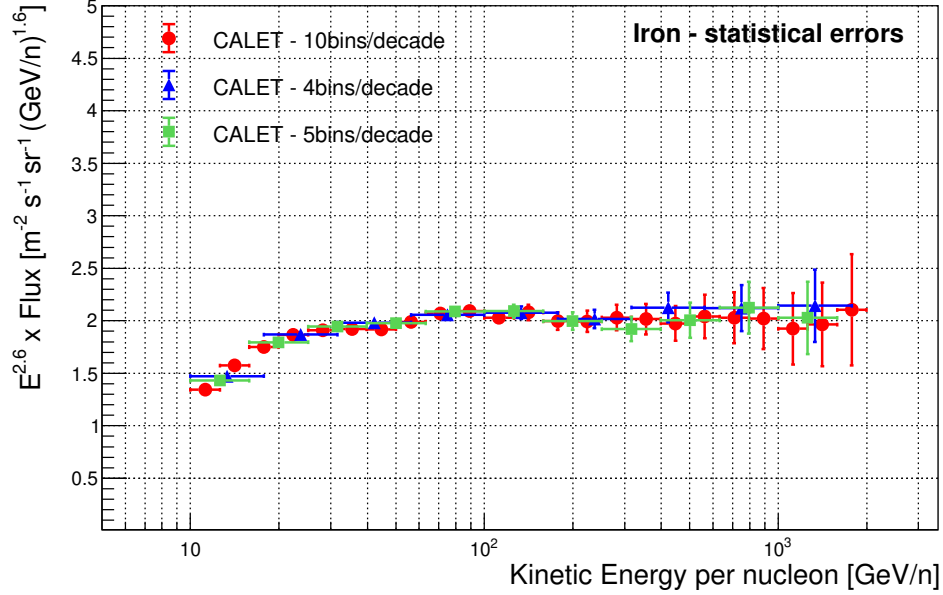


FIG. S9. CALET iron flux with 10 bins/decade (red circles), 5 bins/decade (green squares) and 4 bins/decade (blue triangles). The error bars are representative of purely statistical errors.

the recent AMS-02 measurement [S3], are shown in Fig. S11, as an enlarged version of Fig. 2 in the main body of the paper.

Normalization issues among cosmic-ray flux measurements have a long historical record and unfortunately they seem to persist, in a few cases, also among more recent precision measurements. If we focus on the last 15 years, we notice: (1) an inconsistency of the DAMPE electron flux with AMS-02 in the energy interval from ~ 50 GeV to 1 TeV, whereby the DAMPE electron data are found to be significantly higher than AMS-02 and CALET, the latter being in excellent agreement with each other; (2) an inconsistency of the DAMPE proton flux with AMS-02 (interval from ~ 300 GeV to ~ 1 TeV) and with CALET (from 300 GeV to ~ 10 TeV) where the DAMPE proton flux is significantly higher than the other two experiments; (3) a tension in the AMS-02 normalization (by more than 20%) for carbon flux with respect to PAMELA, CALET and other previous experiments; a similar problem for oxygen with CALET (no oxygen data are available from PAMELA), while preliminary C, O results from DAMPE

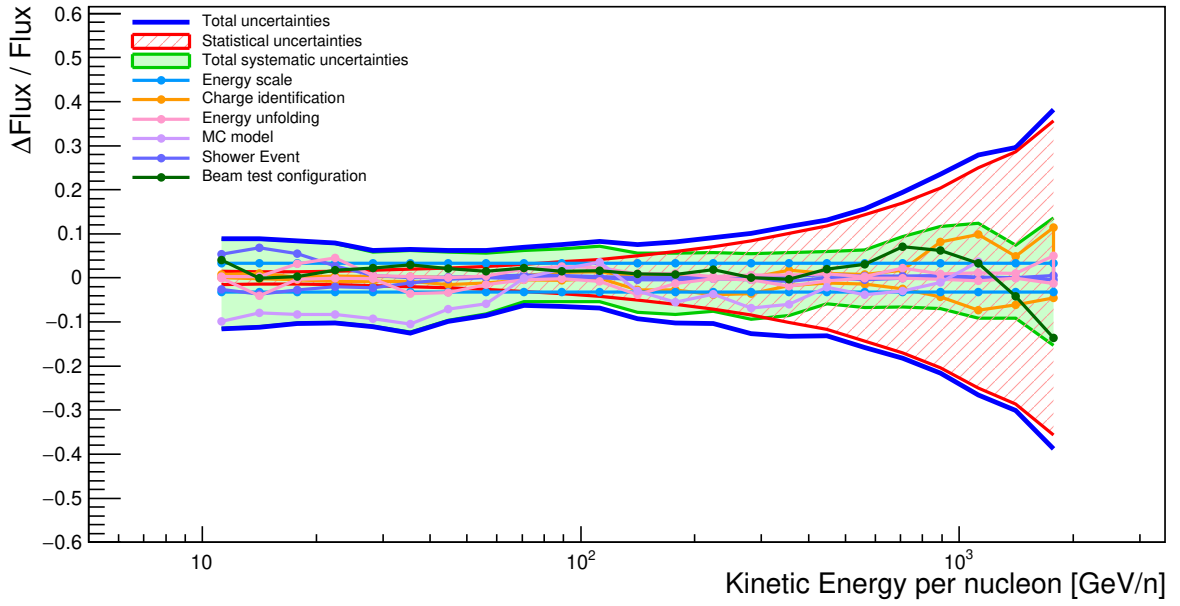


FIG. S10. Energy dependence (in GeV/nucleon) of systematic uncertainties (relative errors) for iron. The band bounded by the red lines represents the statistical error. The shaded band within the green lines shows the sum in quadrature of all the sources of systematics including energy independent ones. A detailed breakdown of systematic energy dependent errors, stemming from charge identification, MC model, energy scale correction, energy unfolding, beam test configuration and shower event shape is shown. The blue lines represent the sum in quadrature of statistical and total systematic uncertainties.

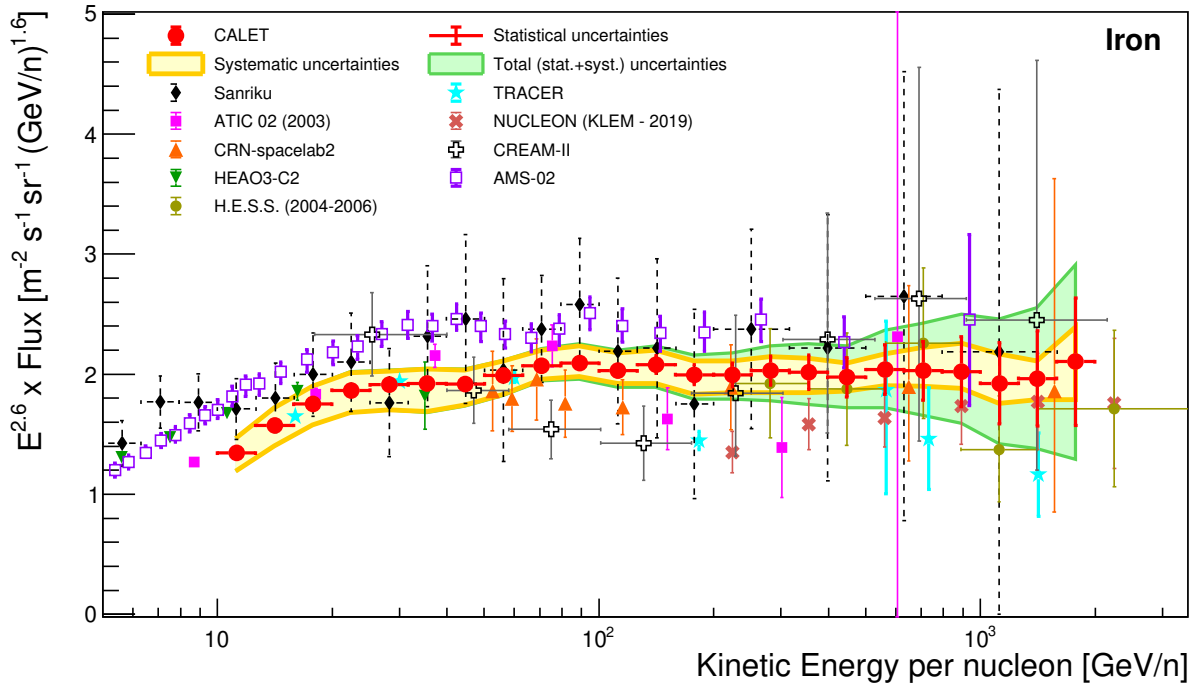


FIG. S11. CALET iron flux as a function of kinetic energy per nucleon in GeV (with multiplicative factor $E^{2.6}$). The error bars of the CALET data (red filled circles) represent the statistical uncertainty only. The yellow band indicates the quadrature sum of systematic errors, while the green band indicates the quadrature sum of statistical and systematic errors. Also plotted are the data points from other direct measurements [S3–S11].

appear to be consistent in normalization with those of AMS-02 (the spectral shape is consistent within the errors for all three experiments); (4) a tension in normalization (by about 20%) between AMS-02 and CALET iron data.

A thorough investigation on possible unaccounted systematic effects related to the normalization of the fluxes has been carried out in the framework of different analyses of CALET with electron, proton, helium, carbon, oxygen, heavier nuclei, and iron data. We partially or totally rule out specific sources of uncertainty. The presence of a significant systematic issue on the live time normalization of the flux is considered unlikely, given the consistency in normalization of the CALET electron, (as well as proton) flux with AMS-02 (and PAMELA) within their respective rigidity ranges. Possible areas where systematic effects could be further investigated by CALET, and by other collaborations as well, include the impact of simulations (specifically on the hadronic cross sections). While EPICS and FLUKA differences were taken into account in the assessment of systematic errors, a comparative study with GEANT4 is not available for CALET at present. Another area under scrutiny is the CALET trigger efficiency. It was extensively studied using ratios of different trigger modes vs the minimum bias trigger and an excellent agreement was found with the MC simulations (see [S12]). The possibility of implementing additional trigger types, and dedicated orbital run modes, to further investigate this aspect is under study.

In figure Fig. S12 the recently published AMS-02 flux is compared with the CALET iron data (with the same multiplicative flux factor $E^{2.7}$), after increasing the latter's overall normalization by 20%. Taking the data at face-value, we notice that the data points of the two experiments not only share a very similar spectral shape, but also have comparable errors.

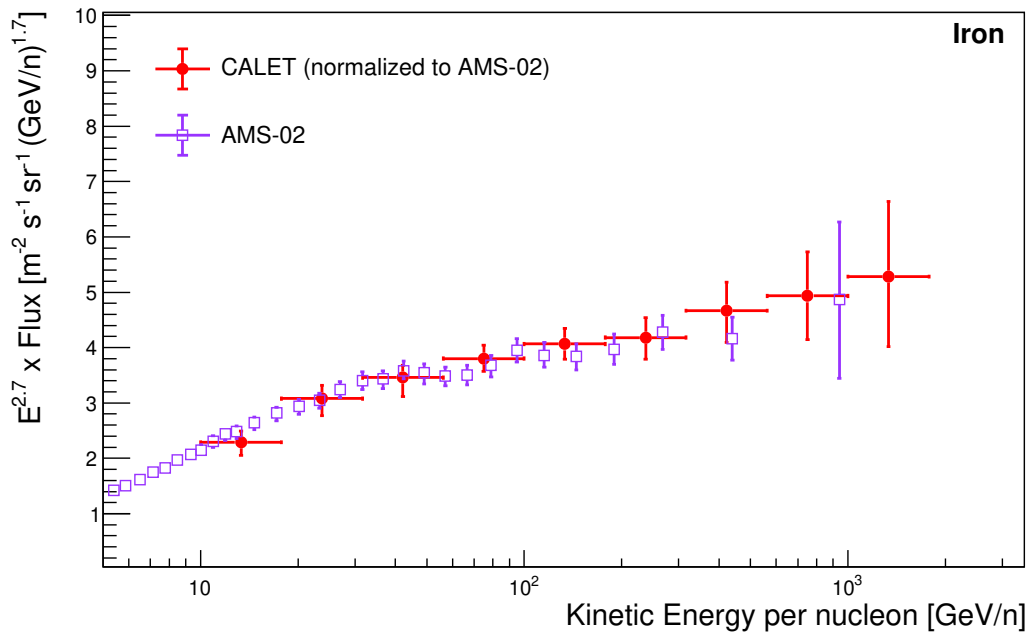


FIG. S12. Iron flux (with multiplicative factor $E^{2.7}$) measured by CALET (red points) with 4 bins/decade, multiplied by 1.20 for comparison with the AMS-02 results [S3]. The error bars of the CALET data are the quadrature sum of statistical and systematic uncertainties.

TABLE I. Table of the CALET differential spectrum in kinetic energy per nucleon of cosmic-ray iron. The first, second, and third error in the flux are representative of the statistical uncertainties, systematic uncertainties in normalization, and energy dependent systematic uncertainties, respectively.

Energy Bin [GeV/ n]	Flux [$\text{m}^{-2}\text{sr}^{-1}\text{s}^{-1}(\text{GeV}/n)^{-1}$]
10.0 – 12.6	$(2.50 \pm 0.03^{+0.14+0.17}_{-0.13-0.25}) \times 10^{-3}$
12.6 – 15.8	$(1.61 \pm 0.02^{+0.09+0.11}_{-0.09-0.16}) \times 10^{-3}$
15.8 – 20.0	$(9.84 \pm 0.10^{+0.53+0.62}_{-0.53-0.85}) \times 10^{-4}$
20.0 – 25.1	$(5.77 \pm 0.06^{+0.31+0.32}_{-0.31-0.50}) \times 10^{-4}$
25.1 – 31.6	$(3.25 \pm 0.04^{+0.18+0.08}_{-0.17-0.31}) \times 10^{-4}$
31.6 – 39.8	$(1.79 \pm 0.03^{+0.10+0.05}_{-0.10-0.20}) \times 10^{-4}$
39.8 – 50.1	$(9.84 \pm 0.16^{+0.53+0.21}_{-0.53-0.79}) \times 10^{-5}$
50.1 – 63.1	$(5.61 \pm 0.11^{+0.30+0.09}_{-0.30-0.35}) \times 10^{-5}$
63.1 – 79.4	$(3.21 \pm 0.07^{+0.17+0.10}_{-0.17-0.02}) \times 10^{-5}$
79.4 – 100.0	$(1.78 \pm 0.05^{+0.10+0.07}_{-0.10-0.01}) \times 10^{-5}$
100.0 – 125.9	$(9.49 \pm 0.28^{+0.51+0.45}_{-0.51-0.08}) \times 10^{-6}$
125.9 – 158.5	$(5.35 \pm 0.19^{+0.29+0.07}_{-0.29-0.30}) \times 10^{-6}$
158.5 – 199.5	$(2.82 \pm 0.12^{+0.15+0.04}_{-0.15-0.18}) \times 10^{-6}$
199.5 – 251.2	$(1.55 \pm 0.08^{+0.08+0.03}_{-0.08-0.08}) \times 10^{-6}$
251.2 – 316.2	$(8.66 \pm 0.52^{+0.47+0.06}_{-0.46-0.66}) \times 10^{-7}$
316.2 – 398.1	$(4.72 \pm 0.34^{+0.26+0.09}_{-0.25-0.31}) \times 10^{-7}$
398.1 – 501.2	$(2.54 \pm 0.21^{+0.14+0.06}_{-0.14-0.06}) \times 10^{-7}$
501.2 – 631.0	$(1.44 \pm 0.15^{+0.08+0.05}_{-0.08-0.06}) \times 10^{-7}$
631.0 – 794.3	$(7.89 \pm 0.95^{+0.43+0.60}_{-0.42-0.31}) \times 10^{-8}$
794.3 – 1000.0	$(4.32 \pm 0.62^{+0.23+0.45}_{-0.23-0.19}) \times 10^{-8}$
1000.0 – 1258.9	$(2.26 \pm 0.40^{+0.12+0.25}_{-0.12-0.17}) \times 10^{-8}$
1258.9 – 1584.9	$(1.27 \pm 0.26^{+0.07+0.06}_{-0.07-0.09}) \times 10^{-8}$
1584.9 – 1995.3	$(7.47 \pm 1.88^{+0.40+0.93}_{-0.40-1.08}) \times 10^{-9}$

-
- [S1] P. S. Marrocchesi *et al.*, Nucl. Instr. and Meth. A **659**, 477 (2011).
[S2] Y. Akaike (CALET), in *Proceedings of Science (ICRC2015) 613* (2015).
[S3] M. Aguilar *et al.* (AMS), Phys. Rev. Lett. **126**, 041104 (2021).
[S4] A. Panov *et al.* (ATIC), Bull. Russian Acad. Sci. **73**, 564 (2009).
[S5] M. Ave *et al.* (TRACER), Astrophys. J. **678**, 262273 (2008).
[S6] H. S. Ahn *et al.* (CREAM), Astrophys. J. **707**, 593 (2009).
[S7] V. Grebenyuk *et al.* (NUCLEON), Adv. in Space Res. **64**, 2546 (2019).
[S8] M. Ichimura *et al.*, Phys. Rev. D **48**, 1949 (1993).
[S9] F. Aharonian *et al.* (H.E.S.S.), Phys. Rev. D **75**, 042004 (2007).
[S10] D. Müller *et al.* (CRN-spacelab2), Astrophys. J. **374**, 356 (1991).
[S11] J. J. Engelmann *et al.* (HEAO3-C2), Astron. Astrophys. **233**, 96 (1990).
[S12] O. Adriani (CALET), Phys. Rev. Lett. **125**, 251102 (2020).